Available online at www.sciencedirect.com
ScienceDirect
International Journal of Mass Spectrometry 261 (2007) 159–169
International Journal of Mass Spectrometry
www.elsevier.com/locate/ijms

Motional coherence during resonance ejection of ions from Paul traps

N. Rajanbabu [a], Anindya Chatterjee [b], A.G. Menon [a,*]

[a] *Department of Instrumentation, Indian Institute of Science, Bangalore 560012, India*
[b] *Department of Mechanical Engineering, Indian Institute of Science, Bangalore 560012, India*

Received 7 July 2006; received in revised form 30 August 2006; accepted 30 August 2006
Available online 17 October 2006

Abstract

We present a study of constraints on pre-ejection dynamical states which cause differential resolution in resonance ejection experiments using Paul traps with stretched geometry. Both analytical and numerical computations are carried out to elucidate the role of damping and scan rate in influencing coherence in ion motion associated with the forward and reverse scan.

Adopting the Dehmelt approximation, our analytical study is carried out on a damped, driven Duffing oscillator with positive octopole nonlinearity. Using the method of multiple scales, we derive approximate slow flow equations which describe the ion motion. The phase portraits generated from the slow flow equations, in the vicinity of the jump, display two stable equilibria (centers) and an unstable fixed point (saddle). Numerical studies on the original equation are used to understand the influence of damping and scan rate in causing coherent ion ejection in these experiments.

In the forward scan experiments, for a given damping, low scan rates result in coherent motion of ions of a given mass at the jump point. At this point, the amplitude and phase of ions of a given mass, starting at different initial conditions, become effectively identical. As the scan rate is increased, coherence is destroyed. For a given scan rate, increasing damping introduces coherence in ion motion, while decreasing damping destroys this coherence.

In reverse scan experiments, for a given damping, very low scan rates will cause coherent ion motion. Increasing the scan rate destroys this coherence.

The effect of damping in reverse scan experiments is qualitatively similar to that in the forward scan experiments, but settling times in the forward scan are shorter, leading to improved coherence and resolution. For mass spectrometrically relevant scan rates and damping values, significantly greater coherence is obtained in the forward scan.

Keywords: Paul trap; Duffing equation; Multiple scales; Coherence; Resonance ejection

1. Introduction

In this paper we study the dependence of resolution on the scan direction in resonance ejection experiments in Paul traps with stretched geometry and in the presence of a buffer gas. In particular, we show how a forward scan direction *constrains* the pre-ejection dynamical states of the ion so as to yield a coherent motion which in turn leads to good resolution, and how a lack of this constraint results in poor resolution spectra in the reverse scan.

Fragment ions of an analyte gas which are confined within the cavity of the three electrode geometry Paul trap mass analyzer (consisting of a ring electrode and two end cap electrodes) oscillate at their secular frequencies, ω_{0u}, in the axial and radial directions. The secular frequencies can be computed by the expression [1,2]

$$\omega_{0u} = \frac{\beta_u \Omega}{2} \tag{1}$$

where u refers to the axial (z) or radial (r) directions, Ω is the angular frequency of the rf drive (applied across the central ring and the two grounded end cap electrodes) and β_u is a parameter related to the Mathieu parameters a_u and q_u. β_u can be obtained using an implicit continuous fraction relationship [1] or more simply, when $q_u < 0.4$, by the expression [3]

$$\beta_u = \sqrt{a_u + \frac{q_u^2}{2}} \tag{2}$$

within the pseudopotential well approximation.

* Corresponding author. Tel.: +91 80 2293 2487; fax: +91 80 2360 0135.
E-mail addresses: nrbabu@isu.iisc.ernet.in (N. Rajanbabu), anindya100@gmail.com (A. Chatterjee), agmenon@isu.iisc.ernet.in (A.G. Menon).

1387-3806/$ – see front matter © 2006 Elsevier B.V. All rights reserved.
doi:10.1016/j.ijms.2006.08.020

In resonance ejection experiments, a fixed frequency ac excitation having sufficient amplitude is applied across the end cap electrodes [4–6]. To resonantly eject the ions from the trap, the secular frequency of the fragment ions is brought into resonance with the fixed frequency excitation by varying the amplitude of the rf drive. In the mass spectrometry literature, increasing the rf amplitude to bring ion secular frequency into resonance with the ac excitation is referred to as the *forward* scan experiment, and decreasing the rf amplitude is referred to as the *reverse* scan experiment [7,8].

Mass spectra obtained by resonance ejection in stretched geometry traps, in the presence of buffer gas, are known to have high resolution in forward scan experiments and relatively poor resolution in reverse scan experiments [8]. A few theoretical studies in the literature have focussed on understanding the dependence of resolution on experimental parameters. Goeringer et al. [7] developed relations for line width as a function of mass, scan rate and bath gas pressure. They modelled the system as a driven harmonic oscillator with damping. Arnold et al. [9], using a similar expression, derived a relationship for the maximum possible resolution at high ion mass-to-charge ratio. Finally, Makarov [10] used a forced, damped Duffing oscillator with positive cubic nonlinearity (corresponding to the stretched trap geometry) and he utilized Mitropol'skii's asymptotic technique [11] to obtain slow flow equations. The fixed points of these equations were used to generate a resonance curve, and a study of that curve, along with detailed numerical simulations, was used to understand resolution and to obtain expressions for the same.

It is at this point that the present paper hopes to contribute. Like Makarov [10], we too model the system to consist of positive octopole nonlinearity, damping and forcing and we consider ion motion to be within the pseudopotential well approximation regime where $q_z < 0.4$. We have taken up for investigation the dependence of resolution on the scan direction through a study of ion dynamics in the neighborhood of resonance. We will demonstrate that the observed resolution in the two directions can be attributed to the constraints on the pre-ejection initial conditions that ions can possess in the forward and reverse scan. It will be seen that coherence of ion motion in the forward scan and the absence of coherence in the reverse scan results in the observation of differing resolutions in the two directions.

In comparison to Makarov's work, ours may be viewed as addressing the following questions. How and when are studies based on the resonance curve valid in the presence of transient motion? How do damping, scan rate and scan direction affect this validity? What are the *mechanisms* responsible for the differential resolutions observed in the forward and reverse scan experiments? In particular, we use phase portraits of the slow flow to investigate these questions, thereby obtaining a qualitative understanding that continues beyond Makarov's treatment. Finally, full, numerical simulations will bear out the validity of the insight obtained from our phase portraits.

2. Equation of motion

The equation of motion of ions in the axial direction in a Paul trap with positive octopole field superposition, damping and dipolar excitation, within the psuedopotential well approximation, is given by [12]

$$\frac{\mathrm{d}^2z}{\mathrm{d}t^2} + c\frac{\mathrm{d}z}{\mathrm{d}t} + \omega_{0z}^2 z + \frac{8f}{r_0^2}\omega_{0z}^2 z^3 = -F_\mathrm{s}\cos\omega t \tag{3}$$

where z is the motion of the ion in the axial direction, t is the time, c is the damping coefficient (which arises on account of helium bath gas), f is the ratio of the weight of octopole superposition with that of quadrupole superposition, r_0 is the radius of the trap, ω_{0z} is the secular frequency of the ion in the axial direction, ω is the frequency of the dipolar excitation and

$$F_\mathrm{s} = \frac{eA_1V_\mathrm{s}}{mr_0} \tag{4}$$

where e is the charge of electron, m is the mass of the ion, A_1 is the weight of the dipole component in the field and V_s is the amplitude of the ac dipolar excitation.

In Eq. (4) we have used the viscous drag model for damping proposed by Goeringer et al. [7] which has the form

$$c = \frac{m_n}{m+m_n}\frac{p}{kT_\mathrm{b}}\frac{e}{2\varepsilon_0}\sqrt{\alpha\frac{m+m_n}{mm_n}}$$

where m_n is the mass of the bath gas, $\alpha = 0.22\times10^{-40}\,\mathrm{F\,m^2}$ is the polarizability of the bath gas, $\varepsilon_0 = 8.854\times10^{-12}\,\mathrm{F/m}$ is the permittivity of free space, T_b is the temperature, p is the pressure of the bath gas in Pascal and k is the Boltzmann constant.

Use of this model is supported by the observation of Major and Dehmelt [13] where it has been recommended that the viscous drag model could be used when the mass of the ion is much larger than that of the neutral gas. However, a recent study by Plass et al. [14] has questioned the validity of this model in the context of typical commercial ion traps and has instead suggested that an elastic collision model would be more appropriate for predicting ion behavior. While, for the purpose of individually accurate predictions, we appreciate the practical point made by Plass et al. [14], we note that analytically incorporating the effect of random infrequent collisions poses a challenge beyond the scope of the present paper.

It needs to be emphasized that in traditional resonance ejection experiments ω in Eq. (3) is in fact kept constant, and what varies when the rf amplitude is ramped is ω_{0z}. In order to modify Eq. (3) to the conventional form (in which the frequency of the forcing function is varied) we introduce dimensionless parameters $\tau = \omega_{0z}t$ and $x = (z/r_0)$ and we obtain

$$\frac{\mathrm{d}^2x}{\mathrm{d}\tau^2} + 2\mu\frac{\mathrm{d}x}{\mathrm{d}\tau} + x + \alpha_3x^3 = F\cos\nu\tau \tag{5}$$

where

$$\mu = \frac{c}{2\omega_{0z}} \tag{6}$$

$$\alpha_3 = 8f \tag{7}$$

$$F = \frac{F_\mathrm{s}}{\omega_{0z}^2 r_0} \tag{8}$$

$$\nu = \frac{\omega}{\omega_{0z}} \tag{9}$$

In Eq. (5) the frequency of the forcing function, ν, is the ratio of the excitation frequency to the secular frequency. Thus, since ω (the forcing frequency in Eq. (3)) is held constant, *forward* scan experiments will result in *decreasing* ν and reverse scan experiments will cause ν to increase. α_3 is the coefficient of the cubic nonlinearity and its sign will determine the nature of the nonlinearity. In our study α_3 is always positive. From Eqs. (6) and (8), we note that the damping coefficient, μ, and the amplitude of the forcing term, F, will vary with the secular frequency, ω_{0z}.

The equation of motion of the ions in a Paul trap is described by the Mathieu equation [3]. In this study, however, we will be using the Duffing equation (Eq. (3)) which is valid in the Dehmelt approximation region corresponding to $q_z < 0.4$. As an aside, it will be instructive to understand how the original Mathieu equation responds to dipolar excitation within the Dehmelt approximation region. We will do this by examining escape velocity of ions at an arbitrarily chosen q_z by a method outlined in Abraham et al. [15]. This study will also give a flavor for the altered stability conditions experienced by the ions in the presence of dipolar excitation.

Fig. 1 is a plot of the escape velocity versus q_z. The escape velocity plots have been generated by assuming an ideal Mathieu equation with an additional force term, the equation having the form

$$\frac{d^2z}{d\tau^2} + (a_z + 2q_z \cos 2\tau)z = F \cos \frac{2\omega}{\Omega}\tau \tag{10}$$

The plots have been made along the $a_z = 0$ axis for an ion trap in which the central ring electrode has a radius of 7 mm. The drive frequency, Ω, has been assumed to be 1 MHz and dipolar excitation frequency, ω, has been fixed at 100 kHz corresponding to a q_z value of 0.2829. The initial position and velocity of the ions, in our simulations, have been chosen as 0 m and 0.0001 m/s, respectively. This initial velocity is sequentially incremented in our computations and maximum ion amplitude, for a specified integration time, is estimated. The velocity that causes ion amplitude to just reach the trap boundary is taken to be the escape velocity of the ion at the chosen q_z [15]. The escape velocity plots in the absence of dipolar excitation (i.e., when $F = 0$), as well as in the presence of force, F, corresponding to dipolar excitation amplitude, V_s, of 100 and 200 mV, are presented in this figure. From Fig. 1 (curve 2), it can be noted that when an excitation voltage of 100 mV is applied, there is a decrease in the escape velocity compared to the escape velocity in the absence of dipolar excitation (curve 1) at the selected q_z. When the excitation voltage is increased to 200 mV the escape velocity reduces to zero, implying that any ion encountering this condition will be unstable and will escape from the trap. Curve 2 corresponds to the condition generally used in collision induced dissociation studies and curve 3 is the condition maintained in resonance ejection experiments.

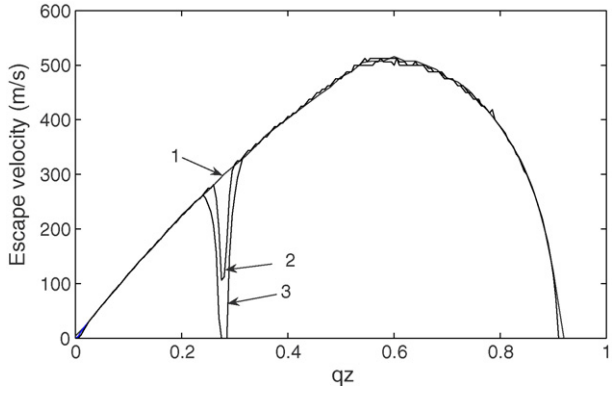

Fig. 1. Escape velocity vs. q_z. (1) Unforced equation, (2) $V_s = 100$ mV, (3) $V_s = 200$ mV.

3. Analytical treatment

We now return to the Duffing equation (Eq. (5)). In order to study the response of the system to variations in damping, nonlinearity, forcing amplitude and frequency we need to derive an analytical expression which captures the dynamics of the system. In the context of the Duffing oscillator, several perturbation techniques have been explored in the mathematical literature. The Lindstedt–Poincaré method and the method of harmonic balance yield only steady state solutions and in our context will not provide an insight into ion dynamics. Two other techniques which can provide us both the transient as well as steady state response are the method of averaging and method of multiple scales. In our study we have used the method of multiple scales [16–19] to derive the relevant slow flow equations. We assume that the coefficients μ, α_3, and F are small. To characterize the smallness of these coefficients, Eq. (5) may be modified as [17]

$$\frac{d^2x}{d\tau^2} + x = \epsilon\left(-2\mu\frac{dx}{d\tau} - \alpha_3 x^3 + F\cos\nu\tau\right) \tag{11}$$

where ϵ is a book keeping parameter. It is also assumed here that the perturbed frequency is close to the natural frequency of the ideal system (in our case $\nu = 1$) and can be represented as

$$\nu^2 = 1 + \epsilon\delta \tag{12}$$

where δ is a detuning parameter. In resonance ejection experiments when the rf amplitude is ramped, we may consider δ to be a function of slow time, T_1, and write

$$\delta = \delta(T_1) \tag{13}$$

where $T_1 = \epsilon\tau$ (discussed below).

Substituting Eq. (12) in Eq. (11) we get

$$\frac{d^2x}{d\tau^2} + \nu^2 x = \epsilon\left(\delta x - 2\mu\frac{dx}{d\tau} - \alpha_3 x^3 + F\cos\nu\tau\right) \tag{14}$$

In the method of multiple scales we define

$$T_0 = \tau, T_1 = \epsilon\tau, \cdots$$

where T_0 is the fast time scale and $T_1, \ldots$ are slow time scales. We assume the solution to Eq. (14) to have the form

$$x(\tau) = X(T_0, T_1, \ldots) \tag{15}$$

where X is assumed to have a form

$$X(T_0, T_1, \ldots) = X_0(T_0, T_1, \ldots) + \epsilon X_1(T_0, T_1, \ldots) + \cdots \tag{16}$$

Further details are summarized in Appendix A. The net result is

$$x \approx A\cos\nu\tau + B\sin\nu\tau \tag{17}$$

and we get

$$\dot{A} = \frac{1}{8\nu}(-8\mu A\nu - 4\delta(\tau)B + 3\alpha_3 A^2 B + 3\alpha_3 B^3) \tag{18}$$

$$\dot{B} = \frac{1}{8\nu}(-8\mu B\nu + 4\delta(\tau)A - 3\alpha_3 A B^2 - 3\alpha_3 A^3 + 4F) \tag{19}$$

by putting $\epsilon = 1$. Eqs. (18) and (19) are the slow flow equations from which we can determine the fixed points of the system. It can be observed that $\dot{A}$ and $\dot{B}$ are dependent on the damping (μ), nonlinearity (α_3) and forcing (F) as well as the detuning (δ). We will be using these equations to generate phase portraits to understand the mechanism of destabilization in resonance ejection experiments.

3.1. Numerical verification

The validity of the slow flow equations obtained above (Eqs. (18) and (19)) to describe the behavior of the original system will be verified by two calculations. In the first, for a given point on the phase portrait, slow changes in the amplitude predicted by the slow flow will be compared with the variation in the amplitude obtained by the integration of the original equation (Eq. (5)). In the second, we compare amplitude response curves obtained from the slow flow equations and the original equation.

The slow flow equations (Eqs. (18) and (19)) are two first order differential equations in the state variables A and B. The time evolution of the solution of the slow flow equations (which is related to the motion of ions) from any initial point can be plotted as a curve on the A–B phase plane and is called a trajectory. A number of such trajectories plotted together is called a phase portrait [20,21]. To generate phase portraits we integrate the slow flow equations for a large number of arbitrarily chosen initial conditions and plot B against A in each case on the same graph.

Fig. 2(a) presents the phase portrait obtained from the slow flow at $\nu = 1.2$ ($\delta = 0.44$) for an undamped condition for an ion of mass 78 Th, an excitation voltage amplitude of 500 mV and for +5% octopole (f) superposition. The slow flow equations are integrated repeatedly for several different initial conditions and phase portraits are generated by plotting A on the x-axis and B on the y-axis. We present this phase portrait in Fig. 2(a) which displays two stable equilibria (centers) marked X and Y, and an unstable equilibrium (saddle) marked Z.

For generating the time response plot (Fig. 2(b)) we choose initial conditions $A = -1.091$ and $B = 0.3146$ corresponding to the point P close to the saddle in Fig. 2(a). For plotting the time response of the original equation we use Eq. (17) to obtain the corresponding initial conditions as $x(0) = -1.091$ and $\dot{x}(0) = 0.3775$. From the phase portrait it can be seen that the trajectory first goes around the low amplitude solution before it swings around the larger amplitude solution. This behavior is reflected in the time response plots in Fig. 2(b). In Fig. 2(b) we also superimpose the variation in amplitude, $R = \sqrt{A^2 + B^2}$,

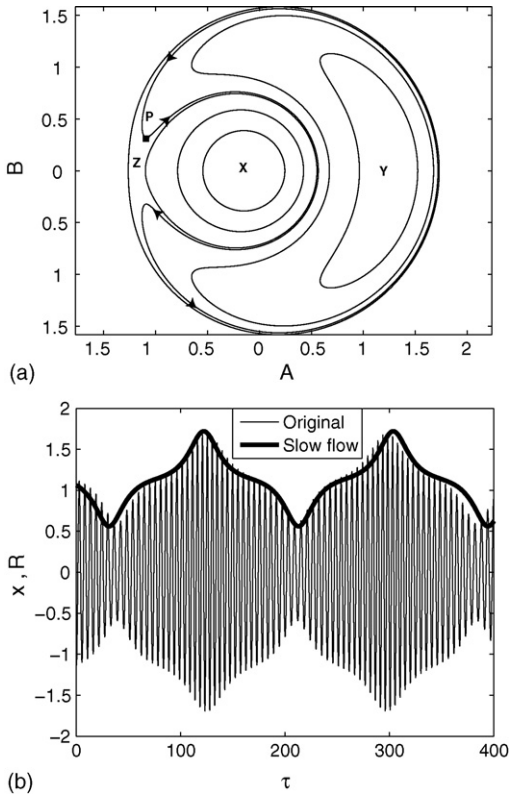

Fig. 2. (a) Phase portrait of the system (Eqs. (18) and (19)) at $\nu = 1.2$ ($\delta = 0.44$), $V_s = 500$ mV, $\alpha_3 = 0.4$, $\mu = 0$. (b) The time response from the original equation and amplitude from the slow flow for the initial condition corresponding to point P on the phase portrait.

obtained by integrating the slow flow equations, as a heavy line. This comparison bears out the validity of the slow flow in approximating the behavior of the original equation.

Note that although the analysis is formally valid for very small δ and α_3, the final match is good even for somewhat large values like $\delta = 0.44$, $\alpha_3 = 0.4$. For smaller values of these parameters, the match will be better.

The phase portrait generated in Fig. 2(a) was for an undamped system and consequently the stable solutions appear as centers in the A–B phase space of Eqs. (18) and (19). In the presence of a buffer gas (damping), when $\mu > 0$, the trajectories in the A–B phase space will eventually settle to one of the fixed points, as shown in Fig. 3.

A second verification of the accuracy of the slow flow to describe our original system is studied through amplitude response curves. An amplitude response curve obtained from the original nonlinear equation (Eq. (5)) is compared with the curve obtained from the slow flow (Eqs. (18) and (19)) in Fig. 4. These curves are generated for an ion of mass 78 Th, pressure of 0.1 Pa, an excitation voltage amplitude of 500 mV and for +5% octopole superposition. The amplitude response curve of the original equation is generated by a simple numerical arc-length based continuation method used by Nandakumar and Chatterjee [22] and is shown by the continuous curve. For obtaining the amplitudes from the slow flow we use $R = \sqrt{A^2 + B^2}$, where A and B are equilibrium values of the first order slow flow equations for different values of ν. The values obtained are indicated by '$*$'. The

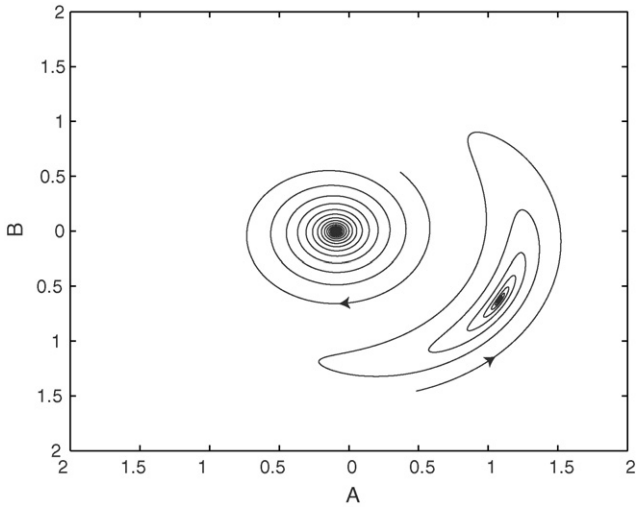

Fig. 3. Phase trajectories of slow flow equations generated for mass 78 Th, $V_s = 500$ mV, pressure = 1 Pa and +5% octopole superposition at $\nu = 1.2$.

trap boundary is indicated by a horizontal line at $R \approx 0.71$ corresponding to z_0/r_0. The amplitudes determined from the slow flow equations closely match those obtained from the original equation, validating the slow flow.

These curves also display the well known jump event observed in systems with cubic nonlinearities [17,23,24]. Jumps are known to occur at the vertical tangents to these curves. In the context of resonance ejection experiments, in the forward scan, at the vertical tangent in the neighborhood of M (Fig. 4), the solution jumps from the lower curve towards the amplitude determined by the upper curve (this has also been pointed out by Makarov [10]) and ions get detected at the trap boundary at this jump point. In reverse scan experiments, however, ion detection occurs when the ion amplitude corresponding to the upper curve reaches the trap boundary and here there is no sudden change in ion amplitude as it happens in the forward scan experiment.

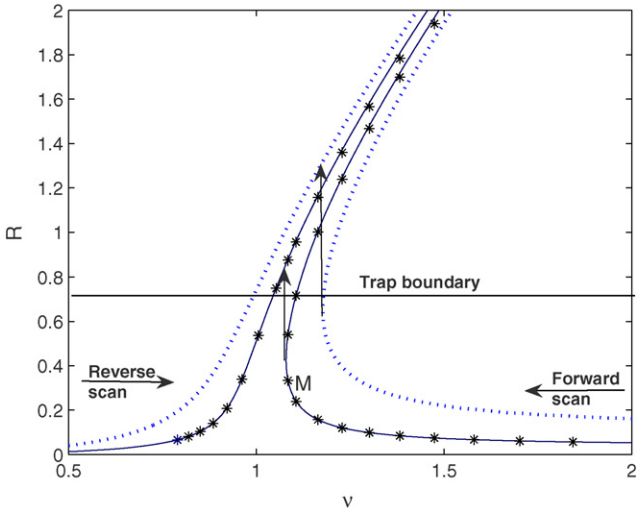

Fig. 4. Amplitude response curve of an ion of mass 78 Th with pressure = 0.1 Pa and +5% octopole superposition. (—) for $V_s = 500$ mV, (···) for $V_s = 1.5$ V, (∗) denotes the amplitude obtained from the slow flow equations.

Also shown in Fig. 4 is the amplitude response curve for larger V_s, to demonstrate that the magnitude of the jump depends on the applied excitation voltage V_s. A larger V_s results in a larger jump (see dotted curve in Fig. 4, made for $V_s = 1.5$ V). Since very small V_s will not make the ion amplitude jump across the trap boundary, a minimum V_s is required for obtaining a spectrum in the forward scan.

4. Results and discussion

It needs to be pointed out that Eq. (5), the Duffing equation, was developed using the pseudopotential well approximation which is valid only for $q_z < 0.4$. In that sense the results we present below are useful only within this range. However, since the discussion we present is *qualitative* in nature we hope this may provide an insight into resonant ion dynamics even at higher q_z values.

As an aside, we point out that the Duffing equation has on occasion been seen to provide useful *quantitative* information at values of q_z greater than 0.4. An example of this is the study of Makarov [10] who used a Duffing equation to develop expressions for line width and resolution which provided very good matches with experimental results at $q_z = 0.86$.

4.1. Phase portraits

We now turn to investigate coherence. For this, we first present the phase portraits derived from the slow flow equations in the region close to resonance. Fig. 5 presents the phase portraits at two different values of ν on the amplitude response curve. These plots have been made for a mass of 78 Th, excitation voltage amplitude of 500 mV and for +5% octopole superposition in the absence of damping.

Fig. 5(a) has been plotted for $\nu = 0.8$ corresponding to $\delta = -0.36$. At this detuning, there exists only one (stable) equilibrium point[1] corresponding to the upper curve of the amplitude response plot. Fig. 5(b) has been plotted for $\nu = 1.2$ corresponding to $\delta = 0.44$. At this detuning, three equilibrium points exist, of which two are stable and the third is unstable. The phase portraits for better understanding, cover amplitudes much larger than the trap dimension. Actually, for Fig. 5(b), the trap physically restricts ion motion amplitudes and so all ion motions are close to the point X. Similarly for Fig. 5(a), ion motion is close to the unique periodic solution. In the presence of damping, moreover, all solutions will settle on to the respective equilibrium points (periodic solutions in terms of the original variable z).

Six more thumb-nail phase portraits are presented in Fig. 6 corresponding to different ν values. Of these, (a) and (b) correspond to regions where the value of ν is smaller than the ν value at the jump point; (c) corresponds to ν value at the jump point and (d), (e) and (f) are the plots for higher ν values. We emphasize that these phase portraits are for zero damping as well as six independently fixed values of δ.

[1] An equilibrium of the slow flow represents a periodic solution in the original z variable.

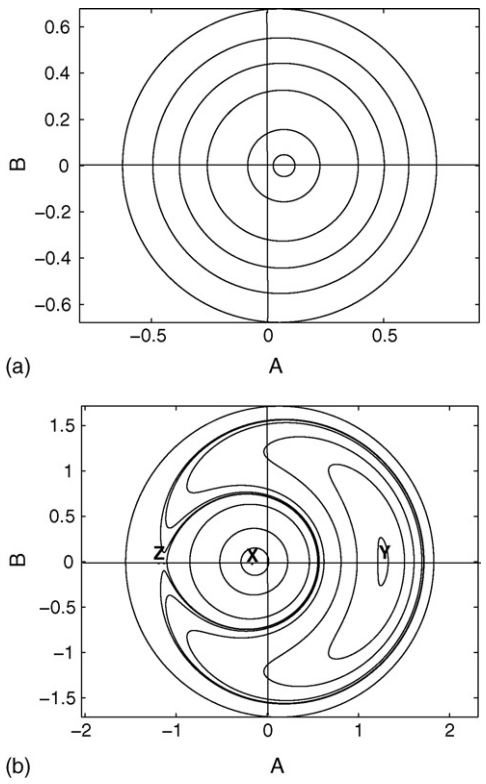

Fig. 5. Phase portraits of the system (Eqs. (18) and (19)) for $V_s = 500$ mV, $\alpha_3 = 0.4$, $\mu = 0$ (no damping) at (a) $\nu = 0.8$ ($\delta = -0.36$) (b) $\nu = 1.2$ ($\delta = 0.44$).

In the phase portraits, at large ν there are three equilibrium points. We have shaded an area of the phase space enclosed by a homoclinic orbit. All trajectories in this area are closed curves representing periodic solutions in A and B (and periodically modulated solutions in the original variable z). In the presence of damping, essentially all of these solutions will settle to equilibrium solution in the middle of the shaded region (amplitude corresponding to the lower curve of the amplitude response plot). As δ varies quasistatically, from a high value to lower values (implying ν varies from higher values to lower values), the area of the shaded region decreases. At the jump point, the area of the shaded region has gone to zero and for an infinitesimally smaller δ the phase portrait displays a single periodic solution with an amplitude corresponding to the upper curve of the amplitude response plot.

In contrast, phase portraits (a) and (b) in Fig. 6 do not display any qualitative change in structure.

4.2. Mass resolution

There are some interesting characteristics associated with the jump point which provide an insight into the improved resolution observed in forward scan experiments. One feature has been presented in the discussion above in relation to Fig. 6, namely, at the jump point ions of the same mass, having different initial conditions at the start of the experiment, have the same amplitude and these ions eject from the trap simultaneously. Another

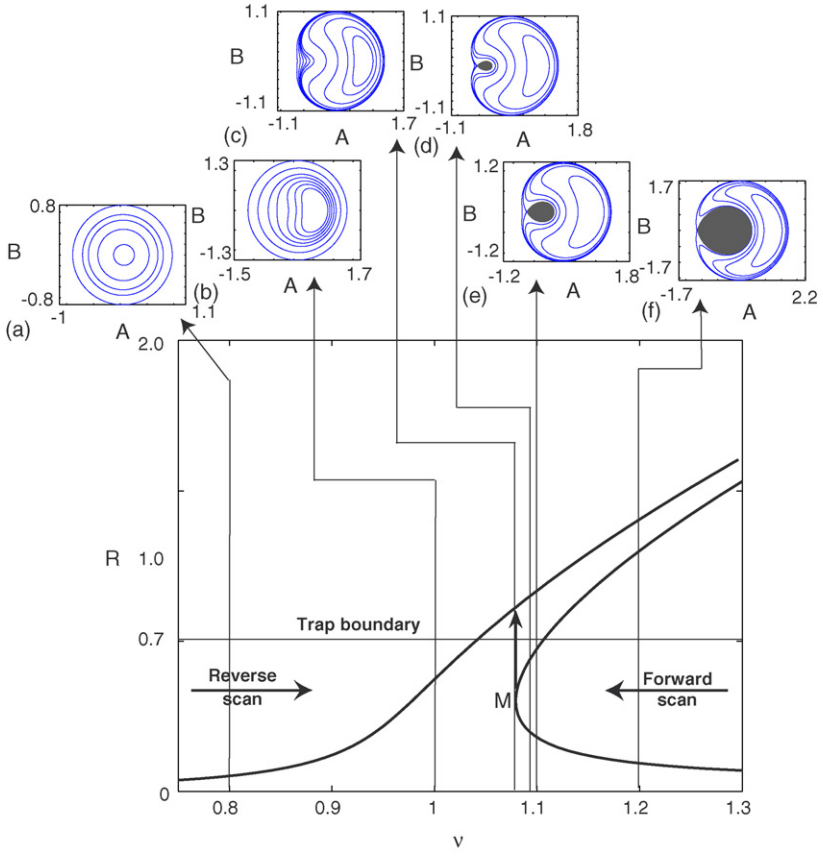

Fig. 6. Amplitude response plots and phase portraits plotted at (a) $\nu = 0.8$, (b) $\nu = 1.0$, (c) $\nu = 1.08$, (d) $\nu = 1.09$, (e) $\nu = 1.1$, (f) $\nu = 1.2$.

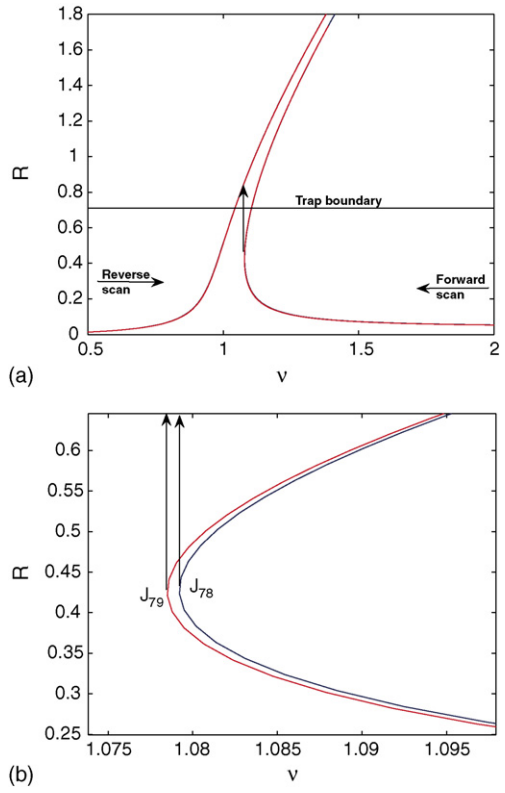

Fig. 7. (a) Amplitude response curves of ions of mass 78 Th and 79 Th with pressure = 0.1 Pa and +5% octopole superposition and V_s = 500 mV. (b) Magnified region close to the jump point.

feature of this curve can be seen in Fig. 7 which has been plotted for identical experimental conditions for two different masses, 78 Th and 79 Th. In Fig. 7(a) the frequency response curves appear to be indistinguishable but the clear separation of the curves is evident in Fig. 7(b) which shows a magnified view of a portion near the jump point of Fig. 7(a). Here, the jump points corresponding to the two masses are labelled J_{78} and J_{79}. This separation determines the ultimate resolution achievable by the mass analyzer. In practice, however, the resolution will be determined by the actual spread in amplitude of the two adjacent masses at the time of jump and, this in turn, will be influenced for a given pressure of the bath gas, by the scan rate.

4.3. Damping, scan rate, and coherence

So far, we have studied the phase portrait with δ = constant (no scan rate) and in the absence of damping. Consider, now, the effect of some damping: it merely causes trajectories within the shaded regions drawn in Fig. 6 to collapse on to the equilibrium point (we ignore delicate issues in resolving what happens to trajectories very close to the original homoclininc orbit, as borderline cases will at most involve a few ions only). As will be seen in the numerical simulations below, the magnitude of damping will determine this rate of collapse and thus will influence resolution in both the forward as well as reverse directions.

Let us now turn to scan rate. Suppose, in addition to damping, there is a very slow but nonzero scan rate. The damped trajectories still have enough time to collapse on to the equilibrium point and then quasistatically follow the equilibrium point as it moves along the appropriate branch of the amplitude response curve (upper or lower, depending on whether it is a reverse or forward scan, respectively). These trajectories therefore remain effectively phase locked with the forcing; all of them have effectively the same amplitude and phase, i.e., the ion motions will be *coherent*; and all are ejected and detected virtually at the same instant, giving good resolution in the spectrum in both directions. However, in traditional resonance ejection experiments such extremely slow scan rates have not been used since very slow scan rates will result in large time delays before detection of high mass ions and this will lead to deterioration of the quality of the spectrum.

Imagine, therefore, we increase the scan rate. There is now a more complex dynamics associated with the ion trajectories (as may be seen by studying the slow flow with a time-varying δ, something we avoid here to maintain focus on the issue of primary interest). Analytically elucidating this complex dynamics would require sophisticated analysis not attempted here; rather, we will use direct numerical integration to elucidate these phenomena in the next section. Here, we present a simple linearized analysis near the periodic solutions which shows that the approach towards the coherent motion is faster during forward scan compared to reverse scan.

Defining $\Theta = \begin{pmatrix} A \\ B \end{pmatrix}$, Eqs. (18) and (19) can be written as

$$\dot{\Theta} = f(\Theta) \tag{20}$$

where

$$f(\Theta) = \begin{pmatrix} f_1 \\ f_2 \end{pmatrix} = \begin{pmatrix} \frac{1}{8\nu}(-8\mu A\nu - 4\delta(\tau)B + 3\alpha_3 A^2 B + 3\alpha_3 B^3) \\ \frac{1}{8\nu}(-8\mu B\nu + 4\delta(\tau)A - 3\alpha_3 A B^2 - 3\alpha_3 A^3 + 4F) \end{pmatrix} \tag{21}$$

Let $\Theta^* = \begin{pmatrix} A^* \\ B^* \end{pmatrix}$ be a fixed point (with δ held constant) of the above system, i.e., $f(\Theta^*) = 0$. For any perturbation about the fixed point Θ^*, $\Theta = \Theta^* + \xi$, we have [25]

$$\dot{\xi} \approx J\xi \tag{22}$$

where J is the Jacobian of $f(\Theta)$ given by

$$J = \begin{pmatrix} \frac{\partial f_1}{\partial A} & \frac{\partial f_1}{\partial B} \\ \frac{\partial f_2}{\partial A} & \frac{\partial f_2}{\partial B} \end{pmatrix} \tag{23}$$

From Eq. (21) we get the Jacobian at Θ^* as

$$J = \frac{1}{8\nu}\begin{pmatrix} -8\mu\nu + 6\alpha_3 A^* B^* & -4\delta + 9\alpha_3 B^{*2} + 3\alpha_3 A^{*2} \\ 4\delta - 3\alpha_3 B^{*2} - 9\alpha_3 A^{*2} & -8\mu\nu - 6\alpha_3 A^* B^* \end{pmatrix} \tag{24}$$

The real part of the eigenvalues of the Jacobian will determine the rate of approach of (A, B) to the fixed point (A^*, B^*). The characteristic equation of J is

$$\lambda^2 - \mathrm{tr}(J)\lambda + \det(J) = 0 \tag{25}$$

and so

$$\lambda = \frac{\mathrm{tr}(J) \pm \sqrt{(\mathrm{tr}(J))^2 - 4\det(J)}}{2}. \tag{26}$$

Assuming low damping, solutions will spiral into (A^*, B^*), therefore λ is complex. The real part of λ is given by

$$\frac{\mathrm{tr}(J)}{2} = -\frac{16\mu\nu}{16\nu} = -\mu \tag{27}$$

But

$$\mu = \frac{c}{2\omega_{0z}} = \frac{c\nu}{\omega} \tag{28}$$

Since c and ω are constants in Eq. (28), the rate of approach of amplitude of ion motion to the fixed point (A^*, B^*), is proportional to ν. In the forward and reverse scan experiments, the ν values are close to each other, with ν being larger for the forward scan case. However, the small difference in ν values is amplified by the larger times involved (many cycles of forcing). Therefore, damping-induced coherence is greater for the forward scan.

Finally, consider the case where the scan rate is high enough to be dynamically far more relevant than the damping. The quasistatic behavior referred to earlier eventually disappears. In such cases, phase locking cannot be expected even in an approximate sense and even in the forward scan direction there will be loss of coherence in ion motion. This occurs primarily due to rate of decrease of amplitude due to damping being much smaller than the scan rate thus resulting in ions not having sufficient time to settle to the stable solution. This, too, will be numerically studied below.

4.4. Numerical simulations

The numerical integration of the original equation (Eq. (5)) has been carried out to study the effect that damping and scan rate have on the resolution in the two scan directions. This study will investigate the response of our system for two initial conditions, viz., $(x(0), \dot{x}(0))$ corresponding to (0.1, 0) and (0.25, 0). In all the plots the y-axis corresponds to the nondimensionalized amplitude. Ejection will occur at $x \approx 0.71$ on this scale. Three damping conditions have been considered and the scan rate is introduced by expressing ν as

$$\nu = \nu_0 + \gamma\tau \tag{29}$$

where ν_0 is the starting value of ν, γ is a dimensionless number akin to the scan rate and τ is dimensionless time. For forward scan the sign of γ is negative and we fix ν_0 as 3 and for reverse scan γ is positive and ν_0 is chosen as 0.1.

The abscissa in these plots correspond to $\nu_0 + 2\gamma\tau$. We briefly explain this choice since in the amplitude response plots in Figs. 4 and 6, the abscissa is ν. To justify this change of independent variable we think of the forcing term $F\cos(\nu\tau)$ in Eq. (5) as $F\cos(\theta)$. Then the abscissa of the amplitude response curve should really be $\dot{\theta}$, i.e., the rate of change of phase in the forcing itself. During a scan, we have

$$\nu = \nu_0 + \gamma\tau; \quad \dot{\nu} = \gamma, \tag{30}$$

and so

$$\dot{\theta} = \nu + \dot{\nu}\tau = \nu_0 + 2\gamma\tau. \tag{31}$$

We have, therefore, plotted $\nu_0 + 2\gamma\tau$ on the abscissa of the time response plots.

We first investigate the effect of damping. For this we fix γ at 0.0005. Figs. 8 and 9 are plots for forward and reverse scan, respectively, for no damping. Figs. 10–12 are the plots for damping corresponding to He bath gas pressure of 0.1 and 1 Pa, respectively. In all these figures subplot (a) corresponds to initial

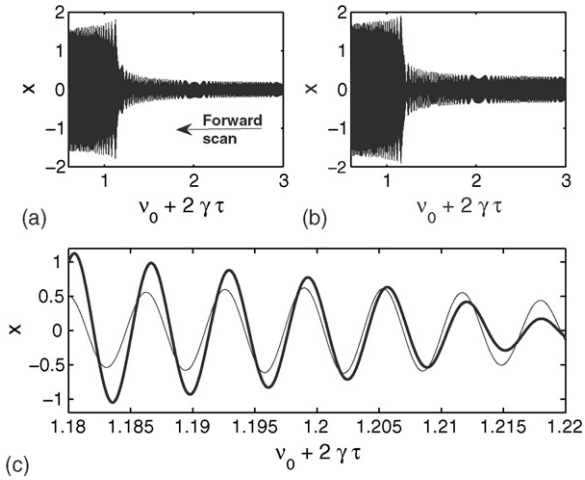

Fig. 8. Time trajectories in the forward scan for initial conditions (a) (0.1, 0) and (b) (0.25, 0), in the absence of damping. $\nu_0 = 3$, $\gamma = -0.0005$. The trajectories for the two initial conditions in the vicinity of the trap boundary ($x \approx 0.7$) are presented in (c). Light curve corresponds to initial condition (0.1, 0) and dark curve corresponds to initial condition (0.25, 0).

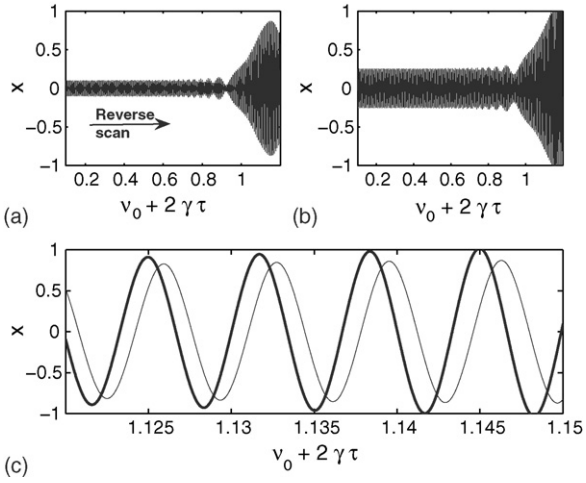

Fig. 9. Time trajectories in the reverse scan for initial conditions (a) (0.1, 0) and (b) (0.25, 0), in the absence of damping. $\nu_0 = 0.1$, $\gamma = 0.0005$. The trajectories for the two initial conditions in the vicinity of the trap boundary ($x \approx 0.7$) are presented in (c). Light curve corresponds to initial condition (0.1, 0) and dark curve to initial condition (0.25, 0).

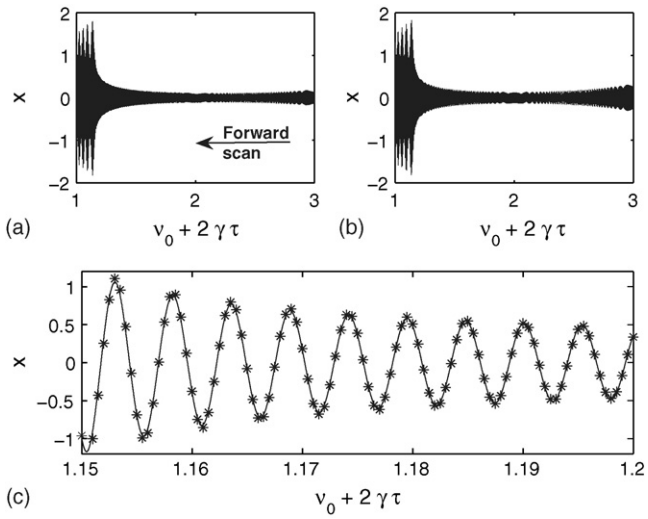

Fig. 10. Time trajectories in the forward scan for initial conditions (a) (0.1, 0) and (b) (0.25, 0), He gas pressure 0.1 Pa, $\nu_0 = 3$, $\gamma = -0.0005$. The trajectories for the two initial conditions in the vicinity of the trap boundary ($x \approx 0.7$) are presented in (c). Continuous curve corresponds to initial condition (0.1, 0) and '$*$' to initial condition (0.25, 0).

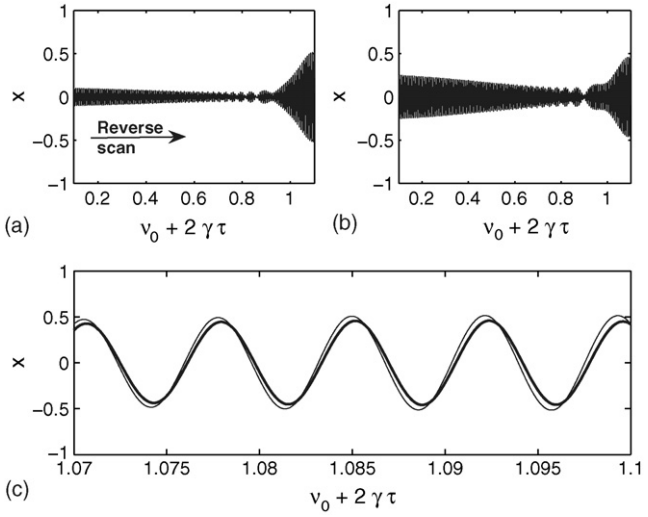

Fig. 12. Time trajectories in the reverse scan for initial conditions (a) (0.1, 0) and (b) (0.25, 0), He gas pressure 1 Pa, $\nu_0 = 0.1$, $\gamma = 0.0005$. The trajectories for the two initial conditions in the vicinity of the trap boundary ($x \approx 0.7$) are presented in (c). Light curve corresponds to initial condition (0.1, 0) and dark curve to initial condition (0.25, 0).

condition (0.1, 0), subplot (b) corresponds to initial condition (0.25, 0) and in subplot (c) we have provided the magnified portion of the plots in (a) and (b) where the amplitude of ion motion crosses the trap boundary. The traces shown in Figs. 9, 11 and 12 for large initial conditions are similar to those presented by Franzen [26] to explain ejection delays caused by multipole superposition in mass selective ejection at the $\beta_z = 1$ stability boundary.

In the absence of damping, trajectories in Figs. 8 and 9 display no coherence in both forward as well as reverse scan. Ions with two different initial conditions, at the start of the experiment, encounter the trap boundary at different values of ν. The situation is dramatically altered in the forward scan in the presence of 0.1 Pa He bath gas pressure. As anticipated from earlier discussions, motion of ions of two different initial conditions fall in step, and they have coherent motion at the approach to the trap boundary. This is demonstrated by the indistinguishable trajectories of the two different initial conditions shown in Fig. 10(c). In the reverse scan, at this pressure, there continues to be lack of coherence as seen in Fig. 11(c). When the He bath gas pressure is further increased to 1 Pa, ion motion in the forward scan continues to be coherent. Although the ion motion in the reverse scan displays greater coherence at 1 Pa when compared to the 0.1 Pascal case, there is still some separation in the trajectories corresponding to the two initial conditions as seen in Fig. 12.

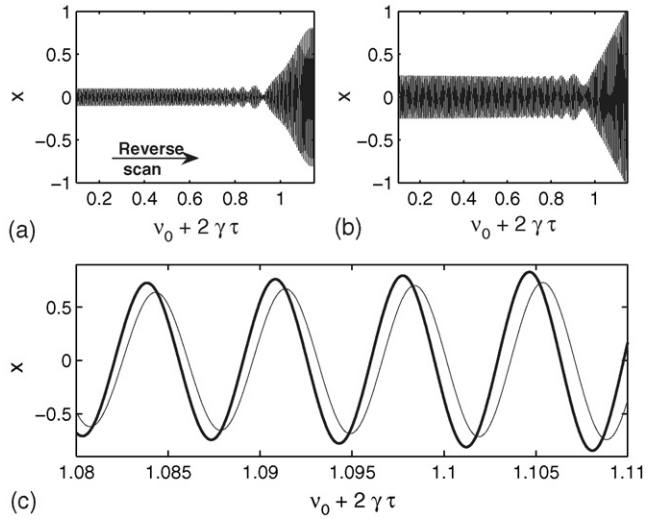

Fig. 11. Time trajectories in the reverse scan for initial conditions (a) (0.1, 0) and (b) (0.25, 0), He gas pressure 0.1 Pa, $\nu_0 = 0.1$, $\gamma = 0.0005$. The trajectories for the two initial conditions in the vicinity of the trap boundary ($x \approx 0.7$) are presented in (c). Light curve corresponds to initial condition (0.1, 0) and dark curve to initial condition (0.25, 0).

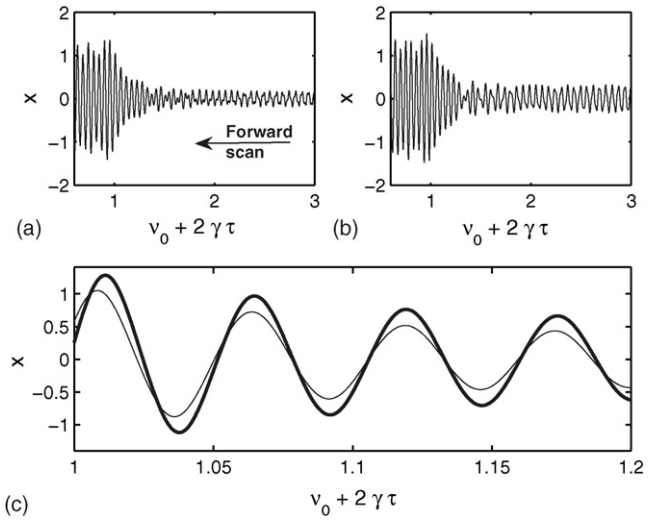

Fig. 13. Time trajectories in the forward scan for initial conditions (a) (0.1, 0) and (b) (0.25, 0), He gas pressure 0.1 Pa, $\nu_0 = 3$, $\gamma = -0.0051$. The trajectories for the two initial conditions in the vicinity of the trap boundary ($x \approx 0.7$) are presented in (c). Light curve corresponds to initial condition (0.1, 0) and dark curve to initial condition (0.25, 0).

To investigate the effect of scan rate, we consider increased scan rate of $\gamma = 0.0051$, corresponding to He bath gas pressure of 0.1 Pa. The time trajectories are presented in Fig. 13. From a comparison of Fig. 10 (which was plotted for $\gamma = 0.0005$) and Fig. 13 it is evident that increasing scan rate has the effect of destroying coherence in the forward direction as has been suggested in our earlier discussion.

5. Conclusions

The motivation of this paper was to understand constraints on the pre-ejection dynamics of ions in the forward and reverse scan resonance ejection experiments. Both analytical and numerical computations have been carried out to understand the cause for the variation in resolution of mass spectra observed in the two scan directions. For our analytical study, ion motion was modelled as a damped, driven Duffing oscillator with positive cubic nonlinearity and, using the method of multiple scales, slow flow equations were derived. These slow flow equations were validated using numerical simulations. Numerical studies have also been carried out on the original Duffing equation to support our qualitative conclusions obtained from the phase portraits.

First confining attention to the amplitude response curve (as done by Makarov [10]) it was observed that the mechanisms of ion ejection in the two scan directions are different. In the forward scan experiment, as previously noted by Makarov, ejection occurs when the ions of a given mass encounter the jump point. At this point, a sudden change in amplitude of ions causes them to get ejected from the trap. In reverse scan experiment, we point out that ion ejection occurs not on account of any jump, but because ion amplitude grows steadily and reaches the trap boundary.

We have, further, studied transient motions away from the amplitude response curve. The role of both damping and scan rate in bringing about coherence in ion motion in the two scan directions has been presented. It is seen that increasing damping leads to coherent ion motion for both scan directions, and decreasing damping leads to loss of coherence. Similarly, very low scan rates result in coherent ion motion in both scan directions and increasing the scan rate destroys the coherence in both directions. However, this effect is larger for reverse scan compared to forward scan. This is because the rate of settling of ions to the periodic motion (coherence) is faster in the forward direction compared to the reverse scan direction.

Finally, we briefly comment on the mechanism proposed in the experimental study reported in Williams et al. [8]. In this paper, they have used the fact that octopole superposition causes the secular frequency of ions to be related to ion oscillation amplitude. Thus in forward scan experiments, the ion secular frequency "runs into" the dipolar excitation frequency causing ejection compacted in time which results in spectra with good resolution. In reverse scan, as ion oscillation amplitude increases, the secular frequency moves away from the dipolar excitation frequency resulting in spectra having poor resolution. The mechanism we have proposed in the present study does not explicitly invoke this amplitude frequency relationship but instead focuses on the constraints on pre-ejection dynamical states to explain the differential resolution. Nevertheless, a shadow of the discussion in Williams et al. [8] may be seen in our discussion in that in one direction a jump is encountered while in the other direction it is not.

Acknowledgements

We gratefully acknowledge Amol Marathe for discussions and T. Pavan for comments on the original manuscript. We would also like to thank two anonymous reviewers for their insightful comments.

Appendix A. Details of multiple scales analysis

We present here the steps involved in the multiple scales analysis of Eq. (11) given in Section 3. Having defined

$$T_0 = \tau,\ T_1 = \epsilon\tau, \ldots$$

the derivatives with respect to τ will become

$$\frac{\mathrm{d}(\cdot)}{\mathrm{d}\tau} = \frac{\partial(\cdot)}{\partial T_0} + \epsilon\frac{\partial(\cdot)}{\partial T_1} + \mathcal{O}(\epsilon^2) \tag{A.1}$$

$$\frac{\mathrm{d}^2(\cdot)}{\mathrm{d}\tau^2} = \frac{\partial^2(\cdot)}{\partial T_0^2} + 2\epsilon\frac{\partial^2(\cdot)}{\partial T_0 \partial T_1} + \mathcal{O}(\epsilon^2) \tag{A.2}$$

Substituting Eqs. (16), (A.1), (A.2) in Eq. (14) and expanding the cubic term, we obtain

$$\frac{\partial^2 X_0}{\partial T_0^2} + \nu^2 X_0 + \epsilon\left[\frac{\partial^2 X_1}{\partial T_0^2} + \nu^2 X_1 + 2\frac{\partial^2 X_0}{\partial T_0 \partial T_1} - \delta X_0 + 2\mu\frac{\partial X_0}{\partial T_0} + \alpha_3 X_0^3 - F\cos(\nu T_0)\right] + \mathcal{O}(\epsilon^2) = 0 \tag{A.3}$$

Collecting the coefficients of ϵ^0, ϵ in Eq. (A.3) we have

$$\frac{\partial^2 X_0}{\partial T_0^2} + \nu^2 X_0 = 0 \tag{A.4}$$

$$\frac{\partial^2 X_1}{\partial T_0^2} + \nu^2 X_1 = -2\frac{\partial^2 X_0}{\partial T_0 \partial T_1} + \delta X_0 - 2\mu\frac{\partial X_0}{\partial T_0} - \alpha_3 X_0^3 + F\cos(\nu T_0) \tag{A.5}$$

We consider the general solution to Eq. (A.4) in the form

$$X_0 = A(T_1)\cos\nu T_0 + B(T_1)\sin\nu T_0 \tag{A.6}$$

where A and B are arbitrary functions of slow time, T_1. Substituting Eq. (A.6) into Eq. (A.5) we get

$$\frac{\partial^2 X_1}{\partial {T_0}^2} + \nu^2 X_1 - 2\frac{\mathrm{d}A}{\mathrm{d}T_1}\sin(\nu T_0) + 2\frac{\mathrm{d}B}{\mathrm{d}T_1}\cos(\nu T_0) - \delta A\cos(\nu T_0) - \delta B\sin(\nu T_0) - 2\mu A\sin(\nu T_0)\nu + 2\mu B\cos(\nu T_0)\nu + \frac{1}{4}\alpha_3 A^3\cos(3\nu T_0) - \frac{1}{4}\alpha_3 B^3\sin(3\nu T_0) + \frac{3}{4}\alpha_3 A^3\cos(\nu T_0)$$

$$+\frac{3}{4}\alpha_3 B^3\sin(\nu T_0)+\frac{3}{4}\alpha_3 A^2 B\sin(3\nu_0)$$
$$-\frac{3}{4}\alpha_3 A B^2\cos(3\nu T_0)+\frac{3}{4}\alpha_3 A^2 B\sin(\nu T_0)$$
$$+\frac{3}{4}\alpha_3 A B^2\cos(\nu T_0)-F\cos(\nu T_0)=0 \quad (A.7)$$

Eq. (A.7) is a nonhomogeneous equation in X_1. The terms involving $\sin(\nu T_0)$ and $\cos(\nu T_0)$ will lead to secular terms (terms whose amplitude grows with time) in the particular solution. In order to eliminate the secular terms from the solution we set the coefficients of $\sin(\nu T_0)$ and $\cos(\nu T_0)$ to zero. When we do so we get the following equations which are the slow flow equations at $\mathcal{O}(\epsilon)$ as

$$\frac{dA}{dT_1}=\frac{1}{8\nu}(-8\mu A\nu-4\delta(T_1)B+3\alpha_3 A^2 B+3\alpha_3 B^3) \quad (A.8)$$

$$\frac{dB}{dT_1}=\frac{1}{8\nu}(-8\mu B\nu+4\delta(T_1)A-3\alpha_3 A B^2-3\alpha_3 A^3+4F) \quad (A.9)$$

From Eq. (A.1), we have

$$\dot{A}=\frac{dA}{d\tau}=\frac{\partial A}{\partial T_0}+\epsilon\frac{\partial A}{\partial T_1}+\mathcal{O}(\epsilon^2) \quad (A.10)$$

and

$$\dot{B}=\frac{dB}{d\tau}=\frac{\partial B}{\partial T_0}+\epsilon\frac{\partial B}{\partial T_1}+\mathcal{O}(\epsilon^2) \quad (A.11)$$

Since the A and B are not functions of T_0, we have

$$\dot{A}=\frac{\epsilon}{8\nu}(-8\mu A\nu-4\delta(\tau)B+3\alpha_3 A^2 B+3\alpha_3 B^3) \quad (A.12)$$

$$\dot{B}=\frac{\epsilon}{8\nu}(-8\mu B\nu+4\delta(\tau)A-3\alpha_3 A B^2-3\alpha_3 A^3+4F) \quad (A.13)$$

References

[1] R.E. March, R.J. Hughes, Quadrupole Storage Mass Spectrometry, Wiley-Interscience Publications, New York, 1989.
[2] R.E. March, Int. J. Mass Spectrom. Ion Process. 118–119 (1992) 72.
[3] P.H. Dawson, Quadrupole Mass Spectrometry and its Application, Elsevier, Amsterdam, 1976.
[4] J.E. Fulford, D.-N. Hoa, R.J. Hughes, R.E. March, R.F. Bonner, G.J. Wong, J. Vac. Sci. Technol. 17 (1980) 829.
[5] R.E. March, A.W. McMahon, E.T. Allinson, A.F. Londry, R.L. Alfred, J.F.J. Todd, F. Vedel, Int. J. Mass Spectrom. Ion Process. 95 (1990) 119.
[6] R.E. March, A.W. McMahon, E.T. Allinson, A.F. Londry, R.L. Alfred, J.F.J. Todd, F. Vedel, Int. J. Mass Spectrom. Ion Process. 99 (1990) 109.
[7] D.E. Goeringer, W.B. Whitten, J.M. Ramsey, S.A. McLuckey, G.L. Glish, Anal. Chem. 64 (1992) 1434.
[8] J.D. Williams, K.A. Cox, R.G. Cooks, S.A. McLuckey, K.J. Hart, D.E. Goeringer, Anal. Chem. 66 (1994) 725.
[9] N.S. Arnold, G. Hars, H.L.C. Meuzelaar, J. Am. Soc. Mass Spectrom. 5 (1994) 676.
[10] A.A. Makarov, Anal. Chem. 68 (1996) 4257.
[11] Y.A. Mitropol'skii, Problems of the Assymptotic Theory of Nonstationary Vibrations, Israel Program for Scientific Translations, Jerusalem, 1965.
[12] S. Sevugarajan, A.G. Menon, Int. J. Mass Spectrom. 209 (2001) 209.
[13] F.G. Major, H.G. Dehmelt, Phys. Rev. 170 (1968) 91.
[14] W.R. Plass, H. Li, R.G. Cooks, Int. J. Mass Spectrom. 228 (2003) 237.
[15] G.T. Abraham, A. Chatterjee, A.G. Menon, Int. J. Mass Spectrom. 231 (2004) 1.
[16] A.H. Nayfeh, Perturbation Methods, Wiley Interscience Publications, New York, 1973.
[17] A.H. Nayfeh, D.T. Mook, Nonlinear Oscillations, Wiley Interscience Publications, New York, 1979.
[18] M.J. Holmes, Introduction to Perturbation Methods, Springer Verlag, New York, 1991.
[19] E.J. Hinch, Perturbation Methods, Cambridge University Press, UK, 1991.
[20] S.H. Strogatz, Nonlinear Dynamics and Chaos, Addison-Wesley, New York, 1994.
[21] R.C. Hilborn, Chaos and Nonlinear Dynamics, Oxford University Press, New York, 1994.
[22] K. Nandakumar, A. Chatterjee, Nonlinear Dyn. 40 (2005) 149.
[23] N.W. McLachlan, Ordinary Non-linear Differential Equations in Engineering and Physical Sciences, Oxford University Press, UK, 1954.
[24] L.D. Landau, E.M. Lifshitz, Mechanics, Third Edition, Pergamon, UK, 1976.
[25] J. Guckenheimer, P. Holmes, Nonlinear Oscillations, Dynamical Systems, and Bifurcations of Vector Fields, Springer Verlag, New York, 1983.
[26] J. Franzen, Int. J. Mass Spectrom. 125 (1993) 165.